

# CFD–DEM Simulations of Current-Induced Dune Formation and Morphological Evolution

Rui Sun, Heng Xiao\*

*Department of Aerospace and Ocean Engineering, Virginia Tech, Blacksburg, VA 24060, United States*

---

## Abstract

Understanding the fundamental mechanisms of sediment transport, particularly those during the formation and evolution of bedforms, is of critical scientific importance and has engineering relevance. Traditional approaches of sediment transport simulations heavily rely on empirical models, which are not able to capture the physics-rich, regime-dependent behaviors of the process. With the increase of available computational resources in the past decade, CFD–DEM (computational fluid dynamics–discrete element method) has emerged as a viable high-fidelity method for the study of sediment transport. However, a comprehensive, quantitative study of the generation and migration of different sediment bed patterns using CFD–DEM is still lacking. In this work, current-induced sediment transport problems in a wide range of regimes are simulated, including ‘flat bed in motion’, ‘small dune’, ‘vortex dune’ and suspended transport. Simulations are performed by using *SediFoam*, an open-source, massively parallel CFD–DEM solver developed by the authors. This is a general-purpose solver for particle-laden flows tailed for particle transport problems. Validation tests are performed to demonstrate the capability of CFD–DEM in the full range of sediment transport regimes. Comparison of simulation results with experimental and numerical benchmark data demonstrates the merits of CFD–DEM approach. In addition, the improvements of the present simulations over existing studies using CFD–DEM are presented. The present solver gives more accurate prediction of sediment transport rate by properly accounting for the influence of particle volume fraction on the fluid flow. In summary, this work demon-

---

\*Corresponding author. Tel: +1 540 231 0926

*Email addresses:* [sunrui@vt.edu](mailto:sunrui@vt.edu) (Rui Sun), [hengxiao@vt.edu](mailto:hengxiao@vt.edu) (Heng Xiao)

strates that CFD–DEM is a promising particle-resolving approach for probing the physics of current-induced sediment transport.

*Keywords:* CFD–DEM, sediment transport, multiphase flow, bedload transport, dune migration

---

## 1. Introduction

The perpetual motion of water carves the surface of the earth by entraining and carrying sediment from one location to another, leading to changes of morphology in the ocean and particularly along the coastline. Scientists rely on fundamental understanding of sediment transport to explain and predict the dynamic evolution of the seabed and coastal bathymetry at various spatial and temporal scales; engineers utilize the understanding of the sediment transport mechanisms to design better civil defense infrastructure, which mitigates the impact of coastal hazards such as storm surges and tsunamis on the coastal communities. However, the understanding and prediction of sediment transport are hindered by the complex dynamics and numerous regimes. Traditional hydro- and morphodynamic models (Delft Hydraulics, 1999; Lesser et al., 2000; Warren and Bach, 1992; Xiao et al., 2010) for sediment transport simulations heavily relied on phenomenological models and empirical correlations to describe sediment erosion and deposition fluxes (Meyer-Peter and Müller, 1948; van Rijn, 1984), which lack universal applicability across different regimes and can lead to large discrepancies in predictions.

With the rapid growth of available computational resources in the past decades, many high-fidelity models have been proposed, including two-fluid models (Hsu et al., 2004; Yu et al., 2012), particle-resolving models (Calantoni et al., 2004; Drake and Calantoni, 2001; Jiang, 1995; Schmeeckle, 2014), and interface-resolving models (Kempe and Fröhlich, 2012; Kempe et al., 2014; Kidanemariam and Uhlmann, 2014a,b). Two-fluid models describe the particle phase as a continuum and thus need constitutive relations to account for the particle–particle collisions and fluid–particle interactions. Particle-resolving models explicitly track the movements of all particles and their collisions, which are thus much more expensive than two-fluid models. Empirical models are still used to compute the fluid–particle interaction

forces. In interface-resolving models, not only individual particles but also the detailed flows fields around particle surfaces are fully resolved. Consequently, they are more expensive than particle-resolving models but require even less empirical modeling.

Particle-resolving models can accurately predict particle phase dynamics such as vertical and horizontal sorting due to densities, sizes, shapes, which are important phenomena in nearshore sediment transport. Possibly constrained by computational resources at the time, early particle-resolving models used highly simplified assumptions for the fluid phase by modeling the fluid as two-dimensional layers (Drake and Calantoni, 2001; Jiang, 1995). The number of particles was also limited to a few thousand particles, and thus the computational domain covers only a few centimeters or less for particle diameters typical for coastal sediments. As a result, these methods were limited to featureless bed under specific flow conditions (e.g., intense sheet flow conditions, where the layer fluid assumption is valid).

### *1.1. Simulation of Sediment Transport with Modern CFD–DEM Methodology*

In the past few years, researchers started to use modern, general-purpose particle-resolving solvers based on Computational Fluid Dynamics–Discrete Element Method (CFD–DEM) to study sediment transport. In CFD–DEM, Reynolds Averaged Navier–Stokes (RANS) equations or Large Eddy Simulations (LES) are used to model the fluid flows, which are coupled with the discrete element method for the particles. The CFD–DEM has been used extensively in the past two decades in the chemical and pharmaceutical industry on a wide range of applications such as fluidized beds, cyclone separator, and pneumatic conveying (Ebrahimi, 2014; Han et al., 2003). On the other hand, special-purpose codes have been used to study specific regimes of sediment transport, where solvers are developed based on and valid for only the sediment transport regime to be studied, e.g., bedload transport under two-dimensional, laminar flow conditions (Durán et al., 2012). However, the use of modern, general-purpose CFD–DEM solvers as those used in chemical engineering applications to simulate sediment transport is only a recent development in the past few years. In his pioneering work, Schmeckle (2014) used an open-source CFD–DEM solver (Goniva et al., 2009; Kloss et al., 2012) to study suspended sediment transport. The merits and significance

of Schmeeckle’s pioneering work are summarized as follows: (1) It is the first work done by using modern CFD–DEM solver in the simulation of sediment transport, especially in the suspended sediment transport regime; (2) Rich data sets are obtained by the CFD–DEM solver that are very difficult to obtain in the field or the laboratory; (3) Several questions of the mechanics of sediment transport are answered, including the mechanisms of saltation and entrainment; (4) Interesting and insightful phenomena are observed, including the increase of bed friction at the transition of suspension. However, a theoretical limitation of his work is that the influence of particle volume fraction on the fluid flow is not considered, since the volume fraction does not appear in the fluid continuity equation (see Eq. (1) in Schmeeckle (2014)). This choice was likely made to avoid the destabilizing effects of the volume fraction on the LES equations. Moreover, the fluid–particle drag law adopted in his work does not explicitly account for the volume fraction. Consequently, the drag law he used is not able to represent the varying shielding effects of particles under different particle loading conditions. This effect is important in particle-laden flows where the flow field has disparate distributions of particle loadings from very dilute to very dense, which is the consensus of the CFD–DEM community (Feng and Yu, 2007; Kafui et al., 2002; Tsuji et al., 1993) in simulating industrial particle-laden flows. Finally, the study by Schmeeckle (2014) focused on suspended sediment on featureless beds with comparison of sediment transport rates to empirical formulas in the literature. Many other regimes of sediment transport such as bedload transport as well as more complex patterns such as the formation and evolution of bedforms are still yet to be studied. Arolla and Desjardins (2015) studied the transport of cuttings particles in a pipe with CFD–DEM, where a volume-filtered LES approach is used to model the fluid flow (Capecelatro and Desjardins, 2013). The emergence of small dunes and sinusoidal dunes from an initially flat particle bed under different flow velocity are observed, demonstrating the capability of CFD–DEM in predicting the stability characteristics of sediment beds. However, quantitative comparisons with experimental data are limited to a few integral quantities such as holding rate, and a more detailed validation with experimental or numerical benchmark data were not performed. In summary, while a few

researchers have made attempts in using CFD–DEM to study sediment transport and have obtained qualitatively reasonable predictions, a rigorous, comprehensive study of sediment transport in a wide range of regimes with detailed quantitative comparisons with benchmark data is still lacking. This study aims to bridge this gap by tackling the unique challenges for the CFD–DEM posed by the physical characteristics of sediment transport problems, which are detailed below.

### *1.2. Unique Challenges of Sediment Transport with CFD–DEM*

Given the decades of experiences of using CFD–DEM in chemical engineering applications, one may expect that all these experiences should be straightforwardly transferable to simulations of sediment transport. Unfortunately, this is not the case. First, most of the critical phenomena such as incipient motion, entrainment, suspension, and mixing of suspended sediments with water occur in a boundary layer near the interface of the fluid and the sediment bed. Adequately resolving the flow features within the boundary layer such as the mean velocity gradient, shear stress, and turbulent coherent structures is essential for capturing the overall dynamics of fluid and particle flows. In contrast, in fluidized bed applications, the dynamics of the fluids and particles in the entire bed are of equal importance. Accurately resolving the boundary layer features poses both theoretical and practical challenges for CFD–DEM. This is because the characteristic length scales of the flow can be comparable to or smaller than the particle diameters, but the CFD–DEM describes the fluid flows with *locally averaged* Navier–Stokes equations, which are only valid at scales much larger than the particle size (Anderson and Jackson, 1967). Moreover, since the carrier phase (water) and the dispersed phase (particles) have comparable densities in sediment transport, many effects that are negligible in gas–solid flows such as added mass effects and lubrication are important sediment transport. In comparison, the density of the carrier phase (air or other gases) in gas–solid flows is two orders of magnitude smaller than that of the particles. Consequently, the fluid–particle interactions are dominated by the drag forces, while the other forces mentioned above are of secondary importance and can be neglected (Zhou et al., 2011).

In this work, we demonstrate that CFD–DEM is able to capture the essential features of sediment transport in various regimes with a small fraction of the computational cost of interface-resolved models. On the other hand, detailed features in the bed dynamics in the turbulent flows are reproduced correctly, which is beyond the reach of lower fidelity models such as two-fluid models or phenomenological model based morphodynamic simulations. Furthermore, we demonstrate that improved results can be obtained by properly accounting for the effects of particle volume fraction on the fluid dynamics and the fluid-particle interaction forces. Therefore, when properly used, CFD–DEM can be a powerful and practical tool to probe the fundamental dynamics of sediment transport across a wide range of regimes.

The rest of the paper is organized as follows. Section 2 presents the theoretical framework of CFD–DEM approach. The technique adopted to address the difficulty of comparable scales between the boundary layer and the particle sizes in sediment transport is introduced. Section 3 summarizes the implementation of the CFD–DEM solver SediFoam and the numerical methods used in the simulations. The results are presented and discussed in Section 4 and 5, respectively. Finally, Section 6 concludes the paper.

## 2. Methodology

### 2.1. Mathematical Model of Particle Motion

In CFD–DEM, the translational and rotational motion of each particle is calculated based on Newton’s second law as the following equations (Ball and Melrose, 1997; Cundall and Strack, 1979):

$$m \frac{d\mathbf{u}}{dt} = \mathbf{f}^{col} + \mathbf{f}^{fp} + m\mathbf{g}, \quad (1a)$$

$$I \frac{d\mathbf{\Psi}}{dt} = \mathbf{T}^{col} + \mathbf{T}^{fp}, \quad (1b)$$

where  $\mathbf{u}$  is the velocity of the particle;  $t$  is time;  $m$  is particle mass;  $\mathbf{f}^{col}$  represents the contact forces due to particle–particle or particle–wall collisions;  $\mathbf{f}^{fp}$  denotes fluid–particle interaction forces;  $\mathbf{g}$  denotes body force. Similarly,  $I$  and  $\mathbf{\Psi}$  are angular moment of inertia and angular velocity of the particle;  $\mathbf{T}^{col}$  and  $\mathbf{T}^{fp}$  are the torques due to contact forces and

fluid–particle interactions, respectively. To compute the collision forces and torques, the particles are modeled as soft spheres with inter-particle contact represented by an elastic spring and a viscous dashpot.

## 2.2. Locally-Averaged Navier–Stokes Equations for Fluids

The fluid phase is described by the locally-averaged incompressible Navier–Stokes equations. Assuming constant fluid density  $\rho_f$ , the governing equations for the fluid are (Anderson and Jackson, 1967; Kafui et al., 2002):

$$\nabla \cdot (\varepsilon_s \mathbf{U}_s + \varepsilon_f \mathbf{U}_f) = 0, \quad (2a)$$

$$\frac{\partial (\varepsilon_f \mathbf{U}_f)}{\partial t} + \nabla \cdot (\varepsilon_f \mathbf{U}_f \mathbf{U}_f) = \frac{1}{\rho_f} (-\nabla p + \nabla \cdot \mathbf{R} + \varepsilon_f \rho_f \mathbf{g} + \mathbf{F}^{fp}), \quad (2b)$$

where  $\varepsilon_s$  is the solid volume fraction;  $\varepsilon_f = 1 - \varepsilon_s$  is the fluid volume fraction;  $\mathbf{U}_f$  is the fluid velocity. The terms on the right hand side of the momentum equation are: pressure gradient  $\nabla p$ , divergence of the stress tensor  $\mathbf{R}$  (including viscous and Reynolds stresses), gravity, and fluid–particle interactions forces, respectively. In the present study, we used large-eddy simulation to resolve the flow turbulence in the computational domain. We applied the one-equation eddy viscosity model proposed by Yoshizawa and Horiuti (1985) as the sub-grid scale (SGS) model. The Eulerian fields  $\varepsilon_s$ ,  $\mathbf{U}_s$ , and  $\mathbf{F}^{fp}$  in Eq. (2) are obtained by averaging the information of Lagrangian particles.

## 2.3. Fluid–Particle Interactions

The fluid-particle interaction force  $\mathbf{F}^{fp}$  consists of buoyancy  $\mathbf{F}^{buoy}$ , drag  $\mathbf{F}^{drag}$ , lift force  $\mathbf{F}^{lift}$ , and added mass force  $\mathbf{F}^{add}$ . Although the lift force and the added mass force are usually ignored in CFD–DEM simulations, they are important in the simulation of sediment transport.

The drag on an individual particle  $i$  is formulated as:

$$\mathbf{f}_i^{drag} = \frac{V_{p,i}}{\varepsilon_{f,i} \varepsilon_{s,i}} \beta_i (\mathbf{u}_{p,i} - \mathbf{U}_{f,i}), \quad (3)$$

where  $V_{p,i}$  and  $\mathbf{u}_{p,i}$  are the volume and the velocity of particle  $i$ , respectively;  $\mathbf{U}_{f,i}$  is the fluid velocity interpolated to the center of particle  $i$ ;  $\beta_i$  is the drag correlation coefficient which

accounts for the presence of other particles. The drag force model proposed by Syamlal et al. (1993) is applied to the present simulations. The lift force on a spherical particle is modeled as (Saffman, 1965; van Rijn, 1984):

$$\mathbf{f}_i^{lift} = C_l \rho_f \nu^{0.5} d_p^2 (\mathbf{u}_{p,i} - \mathbf{U}_{f,i}) \times \nabla \mathbf{U}_{f,i}, \quad (4)$$

where  $\times$  indicates the cross product of two vectors;  $d_p$  is the diameter of the particle;  $C_l = 1.6$  is the lift coefficient. The added mass force is modeled as:

$$\mathbf{f}_i^{add} = C_{add} \rho_f V_{p,i} \left( \frac{D\mathbf{u}_{p,i}}{Dt} - \frac{D\mathbf{U}_{f,i}}{Dt} \right), \quad (5)$$

where  $C_{add} = 0.5$  is the coefficient of added mass.

### 3. Implementations and Numerical Methods

The hybrid CFD–DEM solver *SediFoam* is developed based on two state-of-the-art open-source codes in their respective fields, i.e., a CFD platform OpenFOAM (Open Field Operation and Manipulation) developed by OpenCFD (2013) and a molecular dynamics simulator LAMMPS (Large-scale Atomic/Molecular Massively Parallel Simulator) developed at the Sandia National Laboratories (Plimpton, 1995). The LAMMPS–OpenFOAM interface is implemented for the communication of the two solvers. The solution algorithm of the fluid solver in *SediFoam* is partly based on the work of Rusche (2003) on bubbly two-phase flows. The code is publicly available at <https://github.com/xiaoh/sediFoam> under GPL license. Detailed introduction of the implementations are discussed in Sun and Xiao (2016).

The fluid equations in (2) are solved in OpenFOAM with the finite volume method (Jasak, 1996). The discretization is based on a collocated grid, i.e., pressure and all velocity components are stored in cell centers. PISO (Pressure Implicit Splitting Operation) algorithm is used to prevent velocity–pressure decoupling (Issa, 1986). A second-order central scheme is used for the spatial discretization of convection terms and diffusion terms. Time integrations are performed with a second-order implicit scheme. An averaging algorithm based on diffusion is implemented to obtain smooth  $\varepsilon_s$ ,  $\mathbf{U}_s$  and  $\mathbf{F}^{fp}$  fields from discrete sediment particles (Sun and Xiao, 2015a,b). In the averaging procedure, the diffusion equations are



solved on the CFD mesh. A second-order central scheme is used for the spatial discretization of the diffusion equation; a second-order implicit scheme is used for the temporal integration.

## 4. Results

Simulations are performed using CFD–DEM for three representative sediment transport problems: ‘flat bed in motion’, generation of dunes, and suspended sediment transport. The objective of the simulations is to show the capability of CFD–DEM for different sediment transport regimes. The first two simulations aim to demonstrate that CFD–DEM can capture the features of sediment patterns with a small fraction of the computational cost of interface-resolved method. Therefore, the results obtained are validated with both the numerical benchmark data and experimental results. The purpose of the third simulation is to show the capability of CFD–DEM in ‘suspended load’ regime at high Reynolds number. The results obtained in ‘suspended load’ regime are validated using experimental data.

The numerical setup of the simulations is detailed in Section 4.1. The study of sediment transport in ‘flat bed in motion’ regime is presented in Section 4.2. The generation of ‘small dune’ and ‘vortex dune’ is discussed in Section 4.3. Section 4.4 details the study of sediment transport in ‘suspended particle’ regime.

### 4.1. Numerical Setup

The numerical tests are performed using a periodic channel. The shape of the computational domain and the coordinates system are shown in Fig. 1. The Cartesian coordinates  $x$ ,  $y$ , and  $z$  are aligned with the streamwise, vertical, and lateral directions. The parameters used are detailed in Table 1. The numbers of sediment particles range from 9,341 to 330,000 for sediment transport problems of different complexities.

CFD–DEM is used to study the evolution of different dunes according to the regime map in Fig. 2. This is to demonstrate the capability of CFD–DEM in the prediction of dune migration. It can be seen from the regime map that the dune height increases with Galileo number, which is due to the increase of particle inertia. Simulations at different Galileo numbers are performed to show that CFD–DEM is able to predict the generation of both

‘small dune’ and ‘vortex dune’. It can be also seen in Fig. 2 that the size of the dunes is growing from ‘small dune’ to ‘vortex dune’ then to ‘sinusoidal dune’ with the increase of Reynolds number. However, the influence of Reynolds number to the dune generation is smaller than that of Galileo number.

The geometry of different numerical tests are shown in Fig. 1. The boundary conditions in both  $x$ - and  $z$ -directions are periodic in all cases. For the pressure field, zero-gradient boundary condition is applied in  $y$ -direction. However, there are slight differences in the boundary condition for the velocity field. In Case 1 and 2a, the flow is bounded in the vertical direction by two solid walls and no-slip boundary condition is applied. On the other hand, in Case 2b and 3, the simulations are performed in open channels. In the open channel, no-slip wall is applied at the bottom while free-slip condition is applied on the top. The CFD mesh is refined at the near-wall region and the particle-fluid interface in the vertical ( $y$ -) direction to resolve the flow at the boundary layer. Since the CFD mesh is refined and smaller than the size of sediment particle, a diffusion-based averaging algorithm proposed by the authors (Sun and Xiao, 2015a,b) is applied to average the quantities (volume fraction, particle velocity, fluid-particle interaction force) of Lagrangian particles to Eulerian mesh. The bandwidth  $b$  used in the averaging procedure is  $4d_p$  in  $x$ - and  $z$ - directions and  $2d_p$  in  $y$ -direction. To model the no-slip boundary condition of sediment particles, an artificial rough bottom is applied using three layers of fixed sediment particles. The fluid flow is driven by a pressure gradient to maintain a constant flow rate  $q_f$ . To resolve the collision between the sediment particles, the contact force between sediment particles is computed with a linear spring-dashpot model. In this model, the normal elastic contact force between two particles is linearly proportional to the overlapping distance (Cundall and Strack, 1979). The stiffness, the restitution coefficient, and the friction coefficient are detailed in Table 1. The time step to resolve the particle collision is  $1/50$  the contact time to avoid particle inter-penetration (Sun et al., 2007).

The initialization of the numerical tests follows the numerical benchmark (Kidanemariam and Uhlmann, 2014a) using direct numerical simulations (DNS). The initial positions of the

particles are determined in a separated simulation of particle settling without considering the hydrodynamic forces. In the particle settling simulation, particles fall from random positions under gravity with inter-particle collisions. To initialize the turbulent flow in Case 2b and 3, the simulations first run 20 flow-through times with all particles fixed at the bottom.

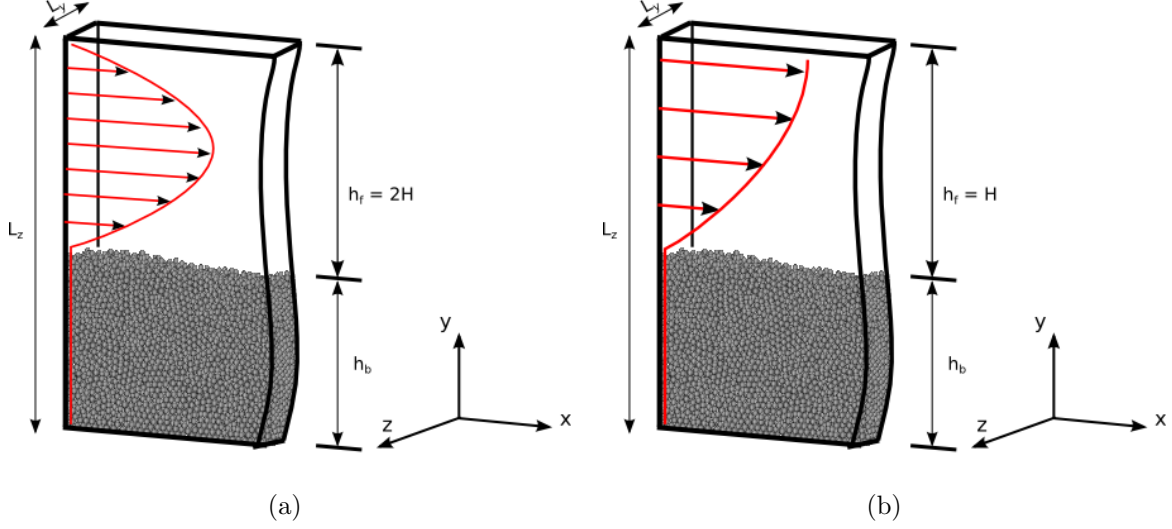


Figure 1: The numerical setup in the simulations. Panel (a) demonstrates the boundary conditions used in case 1 and 2a; Panel (b) demonstrates the boundary conditions used in case 2b and 3.

There are several dimensionless numbers to describe the subaqueous sediment transport. The Galileo number, or the particle Reynolds number, is defined as  $Ga = u_g d_p / \nu$ , where  $u_g = ((\rho_p / \rho_f - 1) |g| d_p)^{1/2}$ . The bulk Reynolds number  $Re_{bulk}$  is given by:

$$Re_{bulk} = \frac{q_f}{\nu} = \frac{2H u_b}{\nu}, \quad (6)$$

where  $q_f$  is the fluid flow rate (note that the volumetric flow rate is divided by the area of the horizontal plane);  $u_b$  is the bulk velocity;  $H$  is the equivalent boundary layer thickness. As shown in Fig. 1, the boundary layer thickness  $H = h_f/2$  in Case 1 and 2a, while  $H = h_f$  in Case 2b and 3. Because the thickness of the boundary layer can be influenced by the height of the sediment bed, there are slight differences in the Reynolds number obtained from the present simulations and the numerical benchmark (Kidānemariam and Uhlmann, 2014a,b).

Table 1: Parameters used in different simulations of sediment transport.

	Case 1	Case 2a	Case 2b	Case 3
bed dimensions				
width ( $L_x$ ) (mm)	16	156	156	120
height ( $L_y$ ) (mm)	12–16	38.4	16.7	40
transverse thickness ( $L_z$ ) (mm)	8	8	40	60
mesh resolutions				
width ( $N_x$ )	16	90	120	120
height ( $N_y$ )	100	100	80	65
transverse thickness ( $N_z$ )	4	6	40	60
particle properties				
total number	9341	79,000	263,000	330,000
diameter $d_p$ (mm)		0.5		
density $\rho_s$ (kg/m <sup>3</sup> )	$2.5 \times 10^3$	$2.5 \times 10^3$	$2.5 \times 10^3$	$2.65 \times 10^3$
particle stiffness coefficient (N/m)	20	200	200	200
normal restitution coefficient	0.3	0.3	0.3	0.01
coefficient of friction	0.4	0.4	0.4	0.6
fluid properties				
density $\rho_f$ (kg/m <sup>3</sup> )		$1.0 \times 10^3$		
viscosity (m <sup>2</sup> /s)	$5.0 \times 10^{-6}$	$1.8 \times 10^{-5}$	$1.5 \times 10^{-6}$	$1.0 \times 10^{-6}$
mean velocity (m/s)	0.12–0.67	0.46	0.34	0.8–1.2
non-dimensional numbers				
bulk Reynolds number $Re_b$	180–1500	840	6500	48000
Galileo number $Ga$	8.6	2.4	28.4	42.9

The fluid height  $h_f$  is defined as  $h_f = L_y - h_b$ , where  $L_y$  is the height of the computational domain;  $h_b$  is the height of sediment bed that is the spatially averaged vertical location of  $\langle \varepsilon_s \rangle = 0.10$ . The Shields parameter  $\Phi$  is defined as  $u_\tau^2/u_g^2$ , where  $u_\tau$  is the shear stress at the bottom. Since the flow is similar to Poiseuille flow in Case 1, the Shields parameter for Poiseuille flow  $\Phi_{Pois}$  is computed from the fluid height  $h_f$ :

$$\Phi_{Pois} = \frac{6Re_{bulk}}{Ga^2} \left( \frac{d_p}{h_f} \right)^2. \quad (7)$$

Additionally, the mean solid volume fraction of the bed is defined as:

$$\varepsilon_{bed} = \frac{1}{y_2 - y_1} \int_{y_1}^{y_2} \varepsilon_s dy, \quad (8)$$

where the interval is taken from  $y_1 = 3d_p$  and  $y_2 = 6d_p$  according to Kidanemariam and Uhlmann (2014b).

#### 4.2. Case 1: Flat Bed in Motion

The regime of the sediment pattern is determined by the Galileo number (Charru and Hinch, 2006). At small Galileo number (typically small particle or large viscosity) the flat bed is stable because the erosion of the sediment bed is dominant. To demonstrate the capability of CFD–DEM in the prediction of the ‘flat bed in motion’ regime, numerical simulations are performed at relatively low Galileo number. Detailed validation of the results obtained by using CFD–DEM is performed.

Table 2 demonstrates the setup of the numerical simulations, which is based on Case BL24 in the study by Kidanemariam and Uhlmann (2014b) with variations in Reynolds number and channel height. Although the physical setup of Case 1a is the same as Case BL24, the fluid height  $h_f$  in the present simulation is slightly larger. This is because the interface-resolved model used ‘contact length’ and enlarged the distance between the sediment particles. Using the ‘contact length’ accounts for the compactness of the seabed but under-predicts the solid volume fraction  $\varepsilon_s$ . Hence, this is not applied in the present simulation.

The sediment flux denotes the average velocity of the sediment particles, which is calculated as follows:

$$q_p(t) = \frac{\pi d_p^3}{6L_x L_z} u_{ave,p}(t), \quad (9)$$

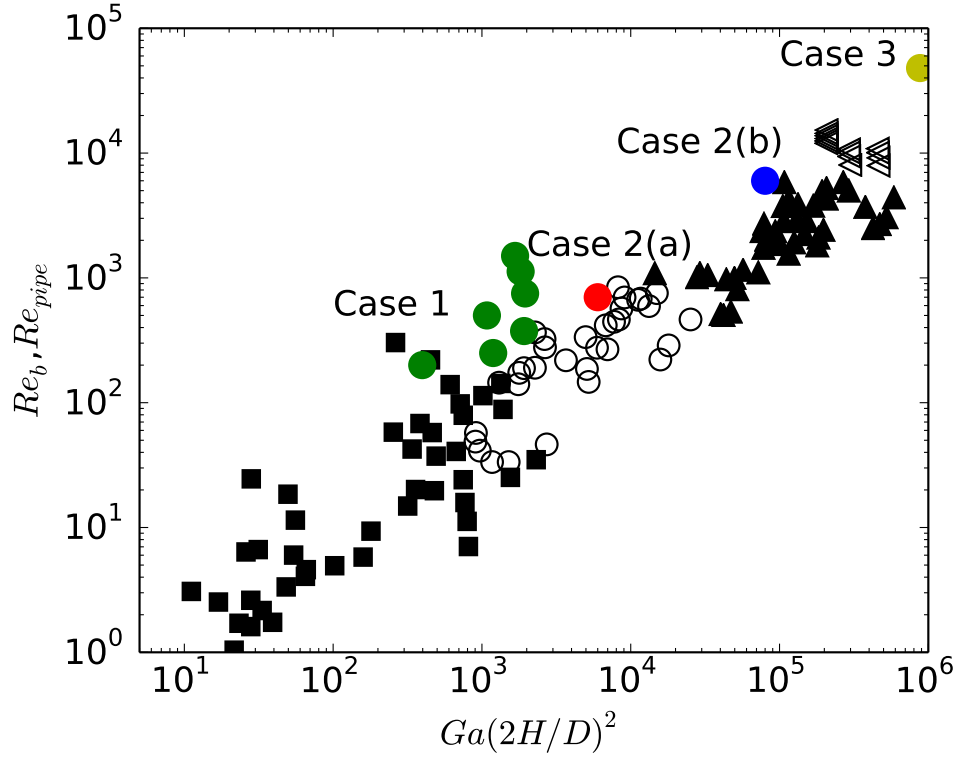


Figure 2: Different patterns observed in the experiments: ‘flat bed in motion’ (■); ‘small dunes’ (○); ‘vortex dunes’ (▲); ‘sinusoidal dunes’ (◁). The green diamonds refer to Case 1; the red triangle refers to Case 2a; the blue triangle refers to Case 2b; the yellow circle refers to Case 3.

Table 2: Parameters used in the simulations of ‘flat bed in motion’

Case	$Re$	$L_y$	$h_f/d_p$	$\Phi_{pois}$	$\varepsilon_{bed}$
Case 1a	375	32	15.0	0.14	0.62
Case 1b	750	32	15.1	0.27	0.62
Case 1c	1125	32	14.6	0.43	0.61
Case 1d	1500	32	14.0	0.63	0.58
Case 1e	250	28	11.8	0.15	0.59
Case 1f	500	28	11.2	0.33	0.63
Case 1g	180	24	6.8	0.32	0.61

where  $q_p(t)$  is the instantaneous sediment flux;  $u_{ave,p}$  is the averaged particle velocity. To normalize the sediment flux, the reference quantity  $q_{visc,D}$  is used (Aussillous et al., 2013):

$$q_{visc,D} = \frac{(\rho_p/\rho_f - 1)gd_p^3}{\nu} = Ga^2\nu. \quad (10)$$

Since  $q_{visc,D}$  is based on the particle diameter  $d_p$ , another quantity  $q_{visc,h}$  accounting for the scale of fluid flow  $h_f$  is used:

$$q_{visc,h} = \frac{(\rho_p/\rho_f - 1)gh_f^3}{\nu} = q_{visc,D} \left( \frac{h_f}{d_p} \right)^3. \quad (11)$$

The time-averaged sediment flux  $q_p$  obtained in the present simulations is shown in Fig. 3 to validate the CFD–DEM model. It can be seen that the sediment flux  $q_p$  normalized by both  $q_{visc,D}$  and  $q_{visc,h}$  are consistent with the trend of the data in the literature. In addition, the sediment flux  $q_p$  predicted by CFD–DEM is consistent with the regression curve proposed by Kidanemariam and Uhlmann (2014b), in which the sediment flux increases cubically ( $q_p/q_{visc,D} = 1.66\Phi_{Pois}^{3.08}$ ). From the experimental results (Aussillous et al., 2013), the critical Shields parameter is  $0.12 \pm 0.03$ . However, in both present study and DNS simulations, the critical Shields parameter is not captured and the sediment transport rate does not decrease significantly below the critical value. This may be attributed to the fact

that critical Shields parameter is defined by visual observation. The averaged height of moving particles  $h_m$  is also demonstrated to evaluate the prediction of streamwise particle motion under the particle-fluid interface. The definition of the moving particles uses the threshold value  $0.005U_f^m$ , where  $U_f^m$  is the maximum flow velocity. It can be seen in Fig. 4 that the averaged height of the moving particles predicted using CFD-DEM is consistent with the results obtained in DNS. The trend of the averaged height  $h_m$  of moving particles obtained in the present simulations is also consistent with the regression curve obtained by Kidanemariam and Uhlmann (2014b), in which the height  $h_m$  is proportional to the square of Shields parameter ( $h_m/d_p = 38.01\Phi_{Pois}^{2.03}$ ). The height of the moving particles is of the order of  $10d_p$  in Case 1d when the Shields number is high.

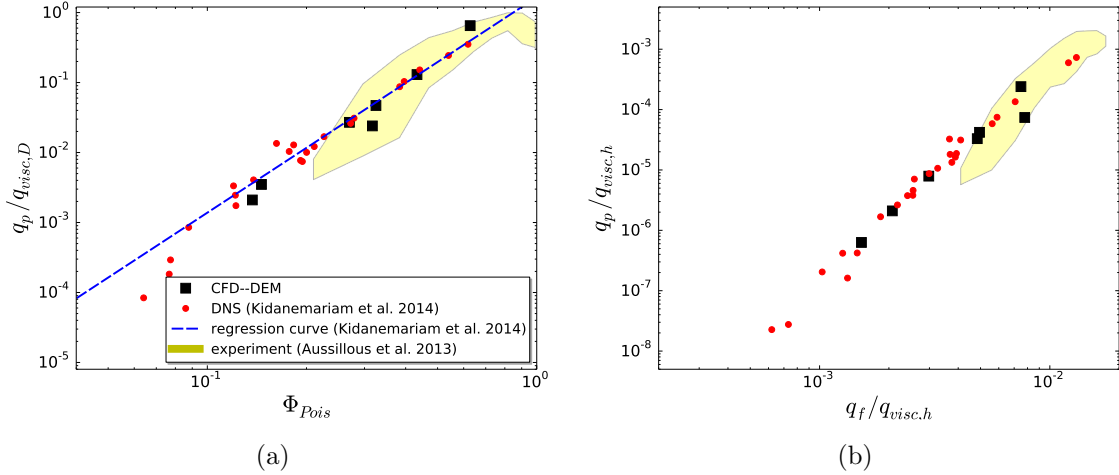


Figure 3: Sediment transport rate obtained in the present simulations. (a) The sediment transport rate normalized by the viscous scaling  $q_{visc,D}$  and plotted as a function of  $\Phi_{Pois}$ ; (b) the sediment transport rate normalized by  $q_{visc,h}$  and plotted as a function of fluid flow rate  $q_f/q_{visc,h}$ .

Another quantity of interest in sediment transport is the velocity of the fluid flow. The flow velocity profiles of Case 1a to Case 1d are shown in Fig. 5(a). The normalized data are plotted in Fig. 5(b): the flow velocity is normalized by the maximum flow velocity  $U_f^m$ , and the distance to the top wall  $\tilde{y} = y - L_y$  is normalized by  $h^*$ , which is the distance



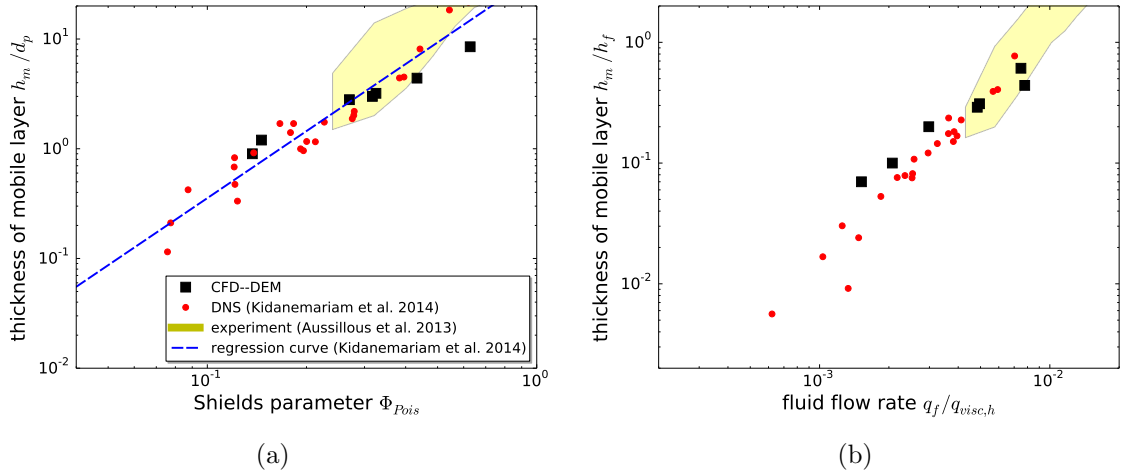


Figure 4: The thickness of mobile layer obtained in the present simulations. (a) The height normalized by the particle diameter  $d_p$  and plotted as a function of  $\Phi_{Pois}$ ; (b) the height normalized by  $h_f$  and plotted as a function of fluid flow rate  $q_f/q_{visc,h}$ .

between the top wall and the location of  $U_f^m$ . It can be seen in Fig. 5(b) that the flow velocity profiles predicted by using CFD-DEM are consistent with the results obtained using interface-resolved method. It is noted that the flow under the fluid-sediment interface is nonzero, which is consistent with the experimental observations (Aussillous et al., 2013). This is an improvement of the DEM-based method over hydro-morphodynamics models, since the hydro-morphodynamics models cannot capture the flow velocity under sediment bed (Delft Hydraulics, 1999; Nabi et al., 2013). Fig. 5(c) demonstrates the relationship of the normalized fluid height  $h_f U_f^m / q_{visc,h}$  and the fluid flux  $q_f / q_{visc,h}$ . At small fluid flux, a linear relationship is observed, which indicates the flow is similar to Poiseuille flow; at relatively large fluid flux the CFD-DEM model captures the deviation of the maximum fluid velocity from Poiseuille flow. The distance  $h^*$  between the top wall and maximum flow velocity  $U_f^m$  can be used to evaluate the influence of sediment bed to the fluid flow. The scattered plot of  $h^*$  as a function of the fluid flux in dimensionless form is shown in Fig. 5(d). It can be seen that the prediction of  $h^*$  are consistent with the experimental data ranging from 0.5-0.7.

To illustrate the motion of the sediment particles in ‘flat bed in motion’ regime, the

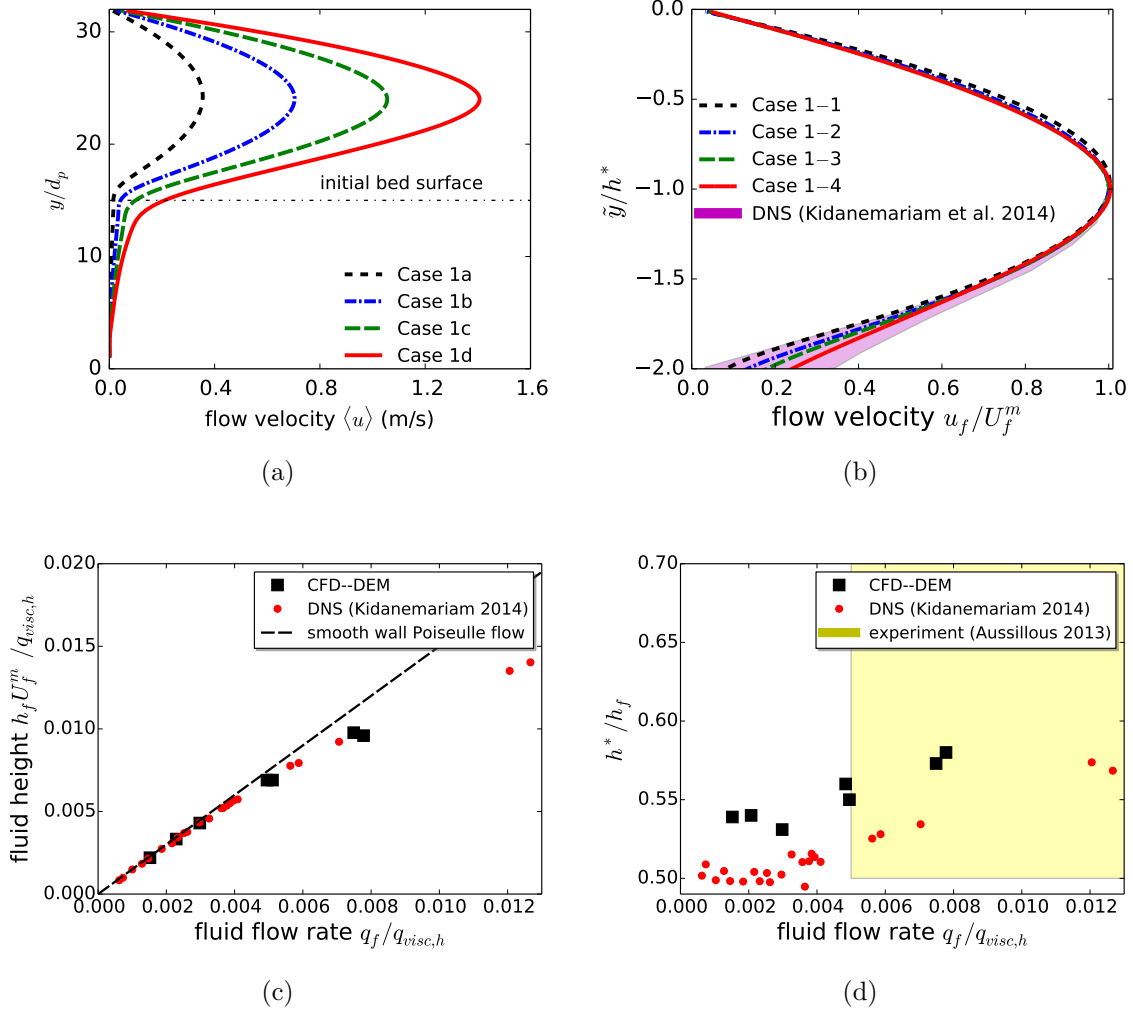


Figure 5: The flow velocity and fluid height obtained in ‘flat bed in motion’ regime. (a) The time-averaged flow velocity profile in the channel; (b) the normalized flow velocity profile by  $U_f^m$ ; (c) the normalized fluid height plotted as a function of fluid flow rate  $q_f/q_{visc,h}$ ; (d) the distance  $h^*$  between the location of  $U_f^m$  and the top wall versus the normalized fluid flow rate.

snapshots of the motion of sediment particles in Case 1b are shown in Fig. 6. The snapshots at  $t_0$  correspond to the start of the saltation and the time interval between the snapshots  $\Delta t = 0.45tU_f^m/L_x$ , which corresponds to 0.45 flow-through times or 1000 DEM time steps. The sliding motion of the particles can be observed according to the change of the locations in the snapshots. To display the particle rotation, the sediment particles are colored half yellow and half red. The yellow halves of the particles are in front at time  $t_0$ , and rotation of the sediment particles can be seen from the change of the orientations. In addition, the saltation of the particle (highlighted in blue) is also shown in Fig. 6. The trace of the blue particle is plotted in the snapshots using the black dash-dot line. It can be seen that the highlighted particle jumps a distance of approximately 10 diameters along the sediment bed at the height of one particle diameter. From the results shown in the snapshots, it can be seen that the sliding, rotation and saltation of sediment particles in bedload are captured by CFD–DEM simulations. Animations of the particle trajectories of Case 1b are provided in the supplementary materials.

#### *4.3. Case 2: Generation of Dunes*

CFD–DEM is used to study the evolution of different dunes according to the regime map in Fig. 2. This is to demonstrate the capability of CFD–DEM in the prediction of dune migration. It can be seen from the regime map that the dune height increases with Galileo number, which is due to the increase of particle inertia. Simulations at different Galileo numbers are performed to show that CFD–DEM is able to predict the generation of both ‘small dune’ and ‘vortex dune’. The results obtained by using CFD–DEM are validated using numerical benchmark and experimental data.

The space-time evolutions of both ‘small dune’ and ‘vortex dune’ are shown in Fig. 7. In this figure, the evolution of sediment patterns obtained by using CFD–DEM are similar with those observed in the study by Kidanemariam and Uhlmann (2014a). The dunes are developed from the perturbations on the flat bed, which is consistent with the observations by Kidanemariam and Uhlmann (2014a). The dune height, wavelength, and the migration velocity of the dunes obtained in the present simulations are demonstrated in Table 3. It

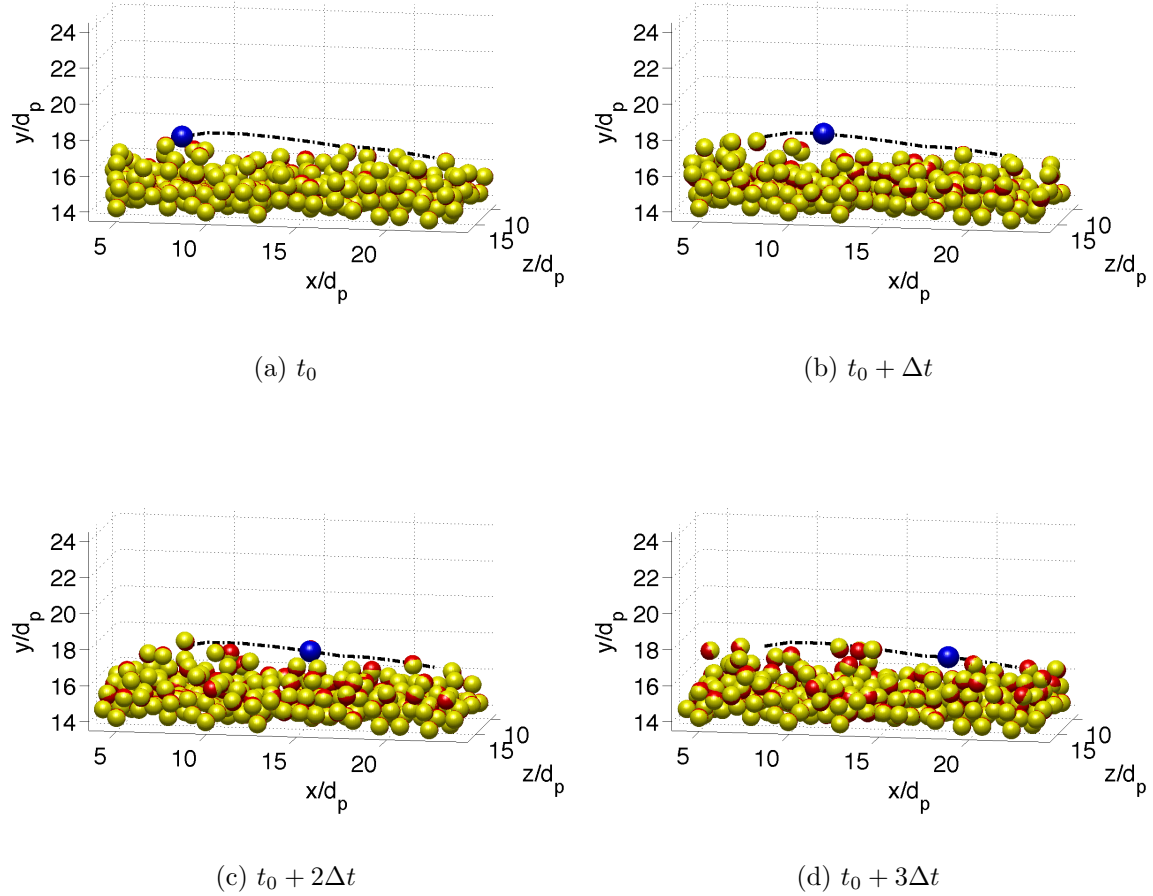


Figure 6: Snapshots of particle locations during the saltation of the highlighted particle (colored in blue). To avoid cluttering, only a portion at the top of sediment bed is shown. The red dash-dot line indicates the trace of particle saltation of the highlighted particle. The particles are colored half yellow and half red to indicate the rotation. Only the particles on the surface are plotted. The time origin ( $t_0$ ) corresponds to the beginning of the cycle and the time interval  $\Delta t = 0.45t_f^m/L_x$ , which corresponds to 0.45 flow-through times or 1000 DEM time steps. The x,y,z axis are normalized by using the particle diameter. Animations of the particle trajectories of are provided in the supplementary materials.

can be seen that the accuracy of CFD–DEM is satisfactory compared with the numerical benchmark and experimental data. Note that the dune migration velocity predicted by using CFD–DEM is smaller than the result obtained by using interface-resolved model. This is because the compactness of the sediment bed in the interface-resolved model is smaller when using the ‘contact length’, and thus the sediment particles are more likely to become suspended and move faster. Since the particles on the crest move more rapidly, the migration velocity of the dune is larger. The snapshot of the dune shape obtained in the present simulations is shown in Fig. 8. It can be seen that both the ‘small dune’ and ‘vortex dune’ generated by using CFD–DEM are geometrically similar with the experimental data obtained by Ouriemi et al. (2009).

The iso-surface of Q-criterion for Case 2b is shown in Fig. 9. It can be seen that CFD–DEM captures the vortex shedding after the dune crests. The vortical structure obtained in the present simulation is consistent with the predictions by Zedler and Street (2001). Additionally, the comparison of Figs. 9(a), 9(b) and 9(c) demonstrates that the number of vortices increases with the height of the dune. This is consistent with the conclusion in the literature that vortical structure is significantly influenced by the dunes (Arolla and Desjardins, 2015; Nabi et al., 2013; Zedler and Street, 2001).

Table 3: Comparison of the dune properties in different tests.

Small dune	present simulation	interface-resolved model	experimental results
dune height	$2d_p$	$2d_p$	$2.5d_p$
wavelength	$156d_p$	$140d_p$	$130d_p$
migration velocity	$0.004u_b$	$0.011u_b$	$0.0024-0.01u_b$
Vortex dune			
dune height	$7d_p$	$5d_p$	$4-8d_p$
wavelength	$156d_p$	$153.6d_p$	$150d_p$
migration velocity	$0.016u_b$	$0.035u_b$	$0.01-0.03u_b$

The sediment transport rates from the present simulations are compared with the experimental data in Fig. 10. It can be seen that the sediment transport rates of both the ‘small dune’ regime and ‘vortex dune’ regime are consistent with the experimental results (Aussilous et al., 2013; Wong and Parker, 2006). This agreement supports the conclusion that the dunes formed at the bottom do not significantly influence the sediment transport rate (Kidanemariam and Uhlmann, 2014a). It is noted that the sediment transport rates obtained in Case 2b is significantly larger than the predictions of Case 2a. This is because the flow regimes of the two test cases are different. In the ‘small dune’ generation test, the particles are rolling and sliding on the sediment bed in laminar flow, and thus there is only bedload. In contrast, in the ‘vortex dune’ case, the flow is turbulent and thus the suspended load contributes to the total sediment flux. In turbulent flow, the sediment particles move much faster than the particles rolling on the sediment bed. Therefore, the sediment transport rate in turbulent flow is larger than that in laminar flow even at the same Shields parameter.

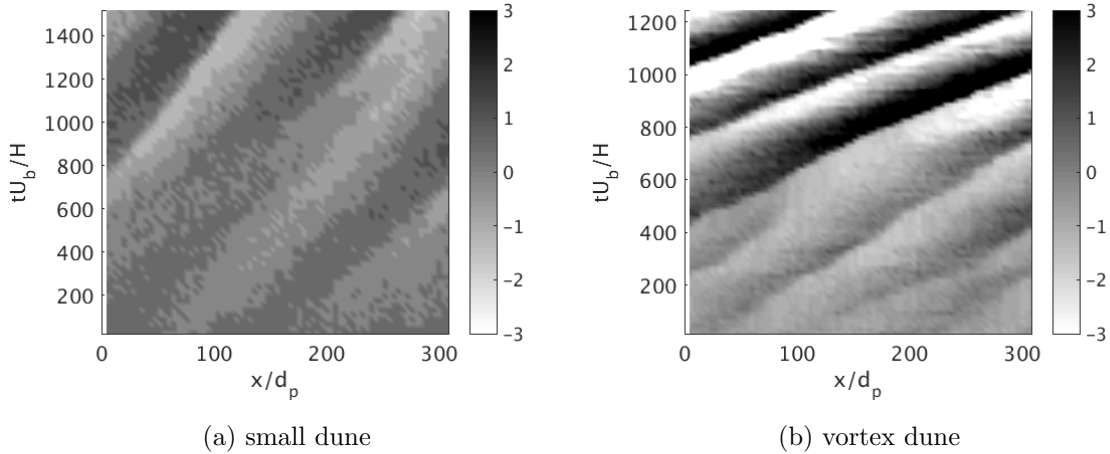
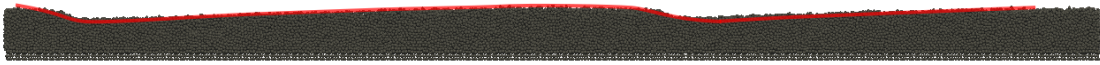
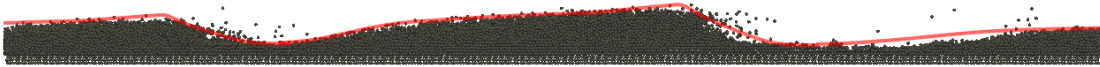


Figure 7: Space-time revolution of the fluid-bed interface  $h' = h(t) - \bar{h}(t)$  for (a) small dune and (b) vortex dune, normalized by the particle diameter  $d_p$ .

In summary, despite some discrepancies, the overall agreement of the results obtained by using *SediFoam* and those in the literature is good. Compared with the computational costs of interface-resolved method ( $5 \times 10^6$  computational hours), the costs of the Case 1b are

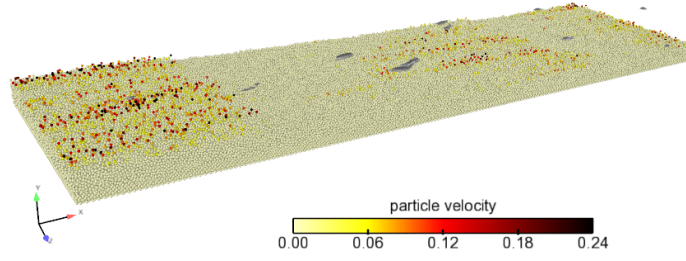


(a) small dune

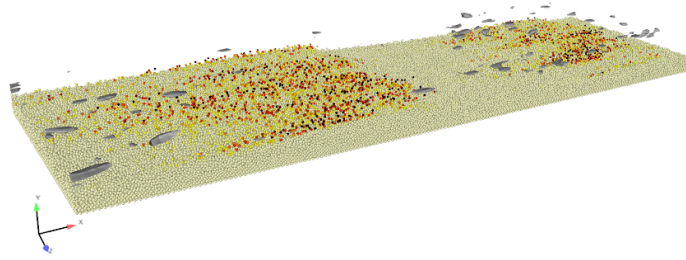


(b) vortex dune

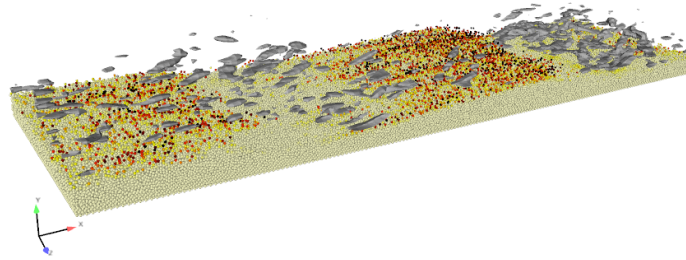
Figure 8: Typical snapshots of the dune shape obtained in present simulations. The black particles denotes the DEM particles; the red curves are geometrically similar to the dunes surfaces obtained from the experimental measurements (Ouriemi et al., 2009).



(a)  $tU_b/H = 560$



(b)  $tU_b/H = 720$



(c)  $tU_b/H = 880$

Figure 9: Vortice after the vortex dune using  $Q$ -criterion at three snapshots. The iso-surface of  $Q = 2000$  is plotted, which is the second invariant of the velocity gradient tensor. The unit of the particle velocity is m/s. The development of the vortical structures is available in supplementary materials.



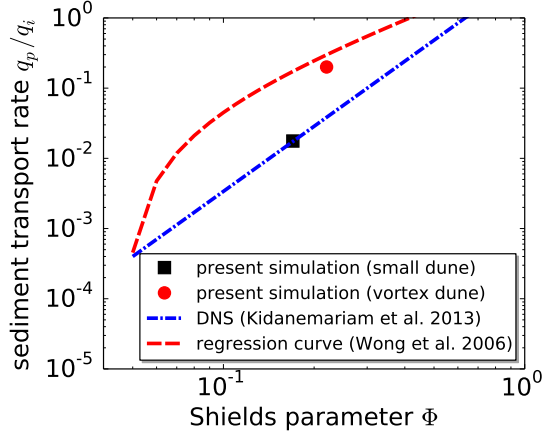


Figure 10: The sediment transport rate  $q_p$ , normalized by  $q_i = u_g d_p$ , of Case 2a and 2b plotted as a function of Shields parameter. The Shields parameter  $\Phi_{pois}$  of Case 2a is defined using Eq. (7); the Shields parameter of Case 2b is defined as  $\Phi = u_\tau^2/u_g^2$ .

only  $2 \times 10^4$  computational hours, which is more than two orders of magnitude smaller. The comparison between CFD–DEM and interface-resolved method suggests that CFD–DEM can predict the movement of dune generation with satisfactory accuracy by using much smaller computational costs.

#### 4.4. Case 3: Suspended Particles

In turbulent flow, if the vertical component of the eddy velocity is larger than the terminal velocity of the sediment particle, the particles become suspended. Simulations are performed to demonstrate the capability of CFD–DEM in ‘suspended load’ regime. In addition, the improvements of the present model over existing simulations using CFD–DEM are presented. The results obtained are only validated using experimental results. This is because the simulations using interface-resolved method are not available in the literature due to the computational costs for high Reynolds number flows.

The domain geometry, the mesh resolution, and the properties of fluid and particles are detailed in Table 1. The flow velocities in three numerical simulations range from 0.8 m/s to 1.2 m/s. The averaged properties of sediment particles are presented in Fig. 11, including the sediment transport rate and the friction coefficient. It can be seen that the sediment

transport rates agree favorably with the experimental data (Nielsen, 1992). It is worth mentioning that the prediction of sediment transport rate  $q_p/q_i$  using *SediFoam* agrees better with the experimental data than the results obtained by Schmeckle (2014). In the present simulations, the shielding effect of particles is considered by accounting for solid volume fraction  $\varepsilon_s$ , and thus the terminal velocity of sediment particles at the seabed is smaller. Since the terminal velocity of the particles is smaller, the particles are more likely to move faster so that the predicted sediment transport rate is larger. The coefficient of friction of the surface is defined as:

$$C_f = u_\tau^2 / \langle u \rangle^2, \quad (12)$$

which describes the hydraulic roughness. As shown in Fig. 11(b),  $C_f$  obtained in the present simulation and by Schmeckle (2014) are larger than the Nikuradse value obtained by using immobile seabed. The increase in  $C_f$  is because the hydraulic roughness over a loose bed is larger in the presence of movable particles (Schmeckle, 2014). Note that the friction coefficient  $C_f$  predicted by *SediFoam* is slightly smaller than the results predicted by Schmeckle (2014). In the present simulation, the volume averaged fluid velocity is obtained by using  $\langle u \rangle = \int_V \varepsilon_f \mathbf{U}_{f,x} dV / \int_V \varepsilon_f dV$ . When the volume fraction term is considered, the fluid volume fraction  $\varepsilon_f < 1$  at the bottom. Since the mean flow velocity at the sediment bed is small, the volume averaged mean flow velocity is larger than that obtained without considering the volume fraction term. Hence, Schmeckle (2014) underestimated the averaged fluid velocity  $\langle u \rangle$ , and thus the friction coefficient  $C_f$  calculated by using Eq. (12) is slightly larger.

The temporally and spatially averaged profiles of sediment volume fraction and normalized fluid velocity at  $U_b = 1.2$  m/s are shown in Fig. 12(a) and 12(b), respectively. It is noted that the solid volume fraction ( $\varepsilon_s$ ) near the bottom obtained in the present simulation is about 0.6, which agrees better with the experimental measurement (Aussillous et al., 2013) than the results obtained by Schmeckle (2014). In the present simulation, the diffusion-based averaging algorithm used no-flux boundary condition to obtain the solid volume fraction  $\varepsilon_s$  at the near-wall region. When using no-flux boundary condition, mass conservation is guaranteed at the wall so that the prediction of volume fraction  $\varepsilon_s$  is more

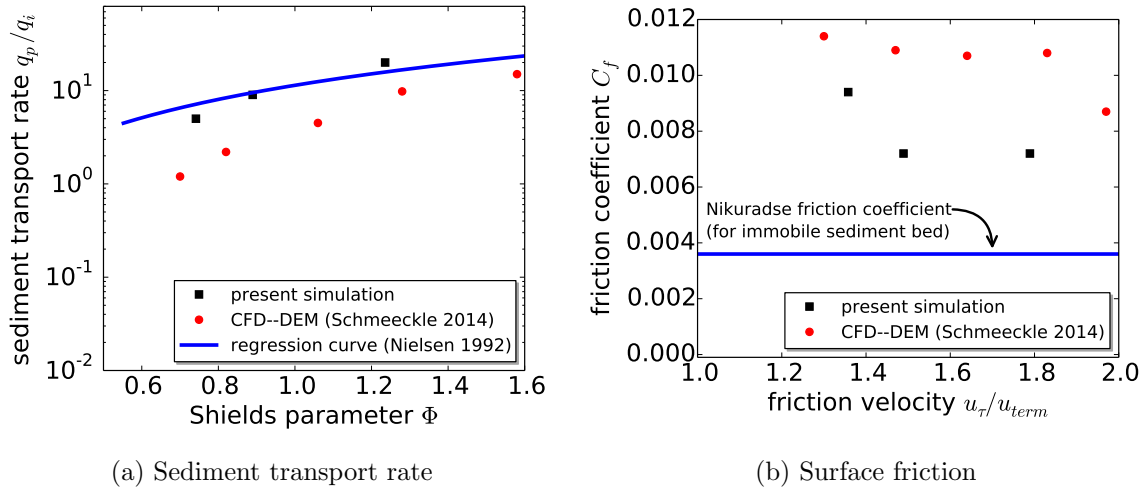


Figure 11: The average properties of the sediment particles. (a) Sediment transport rate; (b) surface friction.

accurate. It can be seen from Fig. 12(b) that the flow velocity obtained in the present simulation follows the law of the wall as obtained in other cases by Schmeeckle (2014). The immobile particle boundary condition at the bottom provides more friction to the sediment particles so that the motion of the bottom particles is constrained. Therefore, the velocity of the fluid flow is smaller due to the drag force provided by the particles. The components of Reynolds stress are shown in Fig. 13. The discrepancies between the Reynolds stresses at the near-wall region is because the bottom particles are fixed so that the flow fluctuation in the present simulation is much smaller. The other turbulent shear stress components  $\langle u'w' \rangle$  and  $\langle v'w' \rangle$  are very small and thus are not omitted in the figure.

A snapshot of the iso-surface using Q-criterion is shown in Fig. 14, which demonstrates the vortical structure in suspend sediment transport. It can be seen that the turbulent eddies are observed at the fluid-particle interface, which is consistent with the results obtained by Schmeeckle (2014). Compared with the vortical structures in the Case 2b, the vortices in suspend load regime are independent from the patterns of the sediment bed. This is because no sediment dunes are generated to change the characteristics of the vortices.

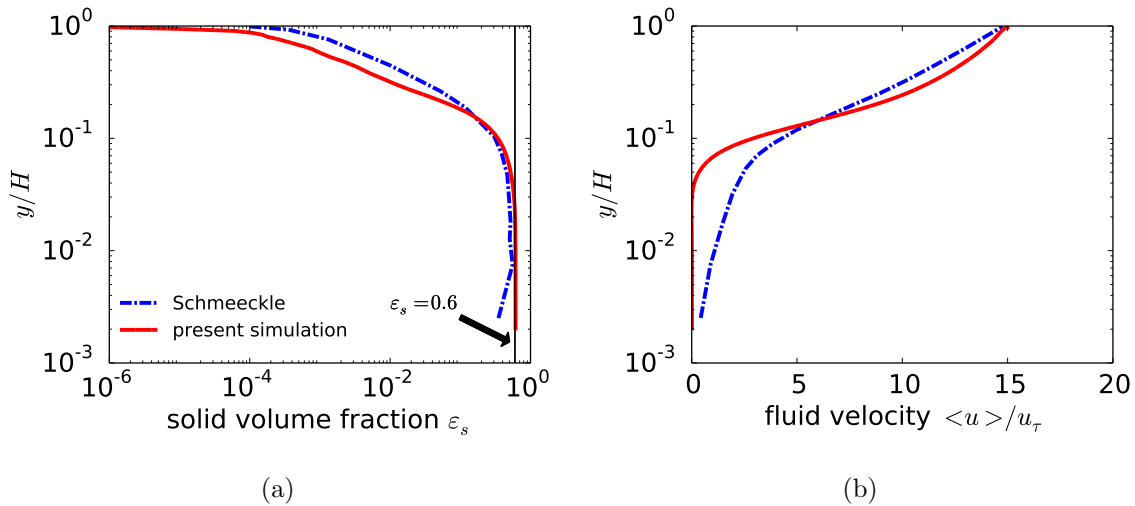


Figure 12: The time-averaged properties of the suspend particles: (a) sediment volume fraction profile; (b) time-averaged velocity profile.

## 5. Discussions

The proof-of-concept study in Section 4 aims to demonstrate that CFD–DEM is able to reproduce the integral or macroscopic quantities of ripple formation and morphological evolution (e.g., wave length, dune height, evolution speed). This validation against experimental data is a prerequisite for performing detailed physical interpretation of the simulation results. Without that, we could risk being misled by numerical artifact of current simulations. However, the investigation of the mechanics in sediment transport is the ultimate goal, and we took advantage of the present CFD–DEM model to investigate the physical insights of sediment transport of different regimes. The discussions on incipient motion in bedload, transition from bedload to suspended load, and coexistence of bedload and suspended load are detailed below.

### 5.1. Interpretations of Parameters Related to Particle Incipient Motion

The critical Shields parameter is defined to describe the criteria for the incipient motion of sediment particles. This value can be determined by employing visual observation or video imaging techniques (Smith and Cheung, 2004) and varies at different Galileo num-

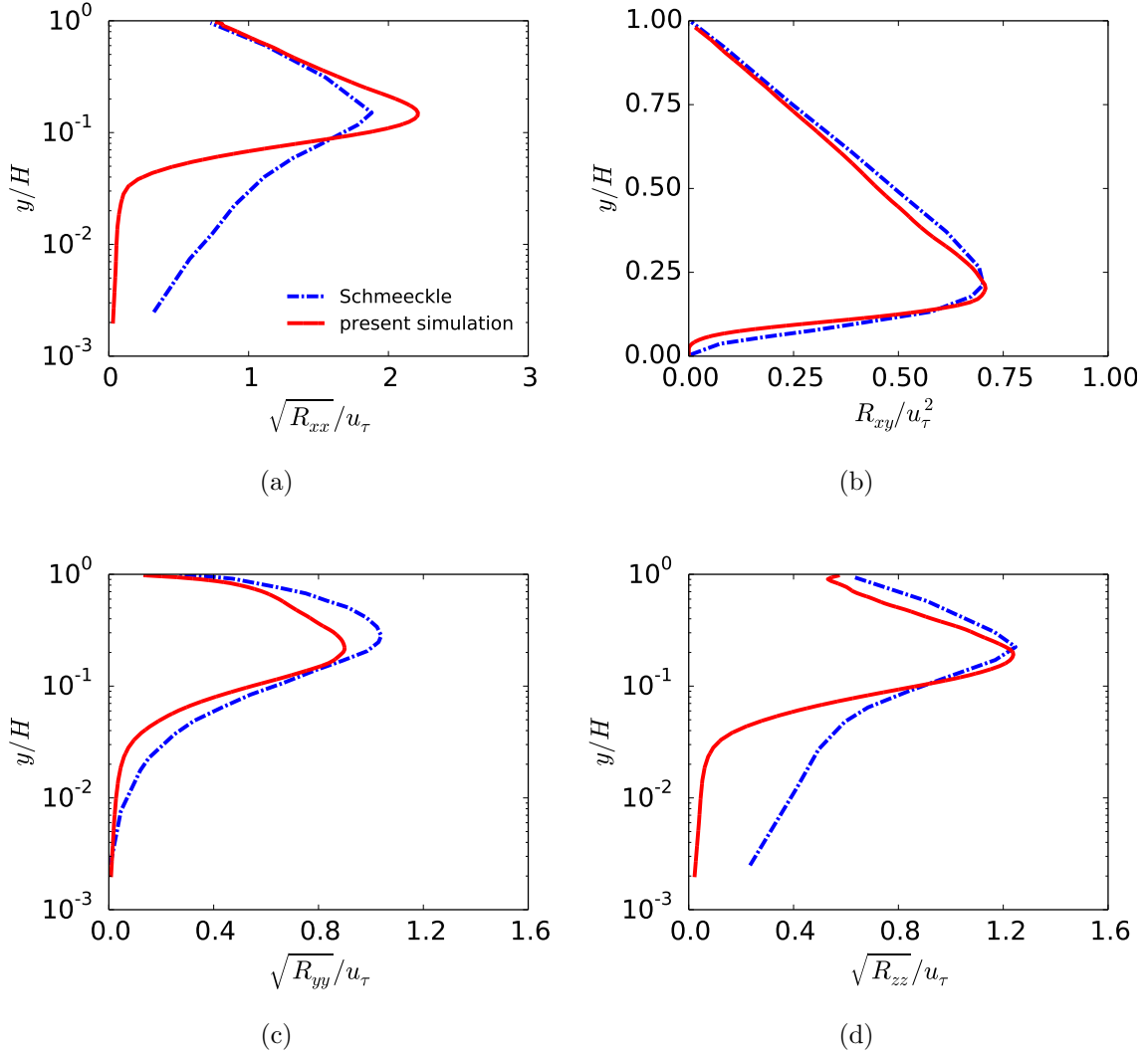


Figure 13: Different components of the temporally and spatially averaged profiles of Reynolds stresses: (a)  $R_{xx}$ , (a)  $R_{uv}$ , (a)  $R_{vv}$ , (a)  $R_{ww}$ .

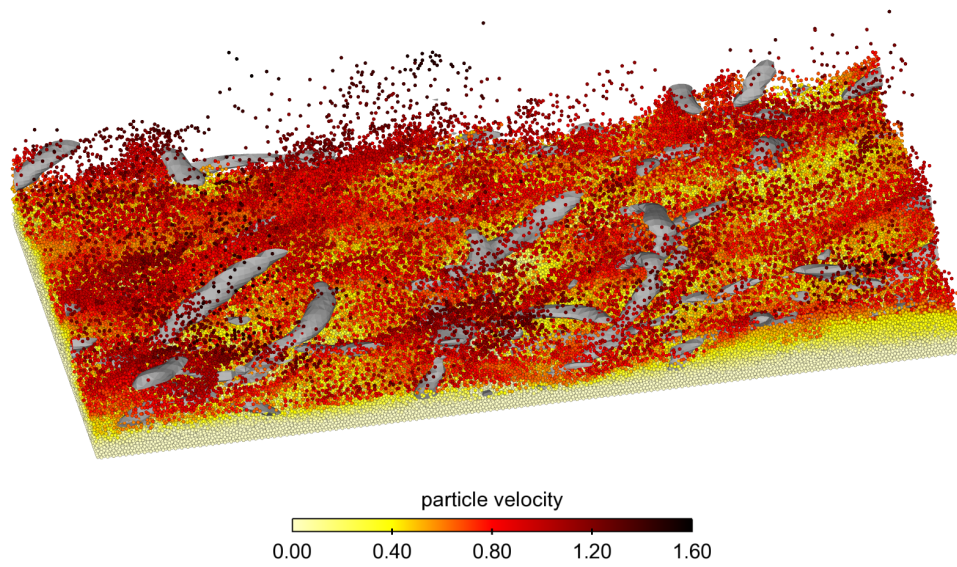


Figure 14: Vortical structures in the suspended particle transport using  $Q$ -criterion. The iso-surface of  $Q = 20000$  is plotted, which is the second invariant of the velocity gradient tensor. The unit of the particle velocity in the figure is m/s.

bers (Brownlie, 1982; Nielsen, 1992). However, the critical Shields stress is not easy to define in terms of the sediment flux  $q_i$ . This is because sediment flux rate decreases gradually and will not totally vanish when the Shields stress decreases, which is supported by both experimental measurement and numerical simulation (Kidanemariam and Uhlmann, 2014a; Smith and Cheung, 2004). The relationship of the Shields stress and the sediment flux in Case 1 is shown in Fig. 15 as an example. The critical Shields stress  $\Phi_{Pois}$  in Poiseuille flow from experimental observation is  $0.12 \pm 0.03$  (Aussillous et al., 2013). However, it can be seen in the figure that there is no sudden change in the sediment flux near the critical Shields stress for both CFD–DEM and DNS simulations. The results obtained in our simulations are consistent with previous findings (Kidanemariam and Uhlmann, 2014a; Smith and Cheung, 2004) that it is difficult to define the minimum flux  $q_{min}$  for incipient sediment motion.

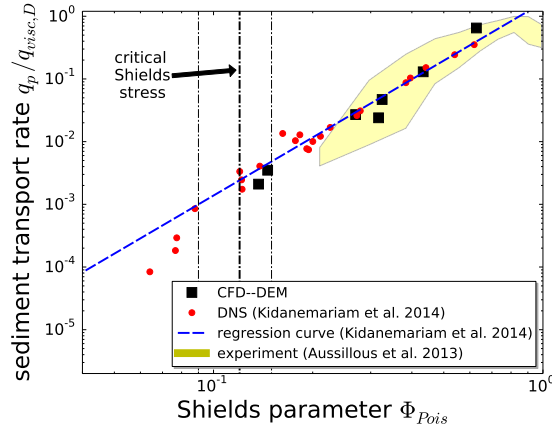


Figure 15: The sediment transport rate of Case 1 plotted as a function of the Shields parameter. The vertical dash-dot lines indicate the range of the Shields parameter.

## 5.2. Transition from Bedload to Suspended Load

The Bagnold criterion for suspension (Bagnold, 1966) denotes the threshold for the transition from bedload to suspended sediment transport. To study this transition, numerical simulations are performed based on the setup of Case 3 by using flow velocities ranging from 0.3 m/s to 1.2 m/s. The sediment transport rate is plotted as a function of the friction velocity in Fig. 16. It can be seen in the figure that the particles become suspended when

the friction velocity at the sediment bed is larger than fall velocity. This is consistent with Bagnold criterion for suspension. Moreover, according to the observation from present simulations, the transition from bedload transport to suspended load is not abrupt but gradual. In bedload regime, when the friction velocity is approaching the Bagnold criterion, dunes are observed. If the friction velocity further increases, the dunes first grow, and then gradually disappear due to the erosion of flow. When the friction velocity is larger than the fall velocity, particles become suspended.

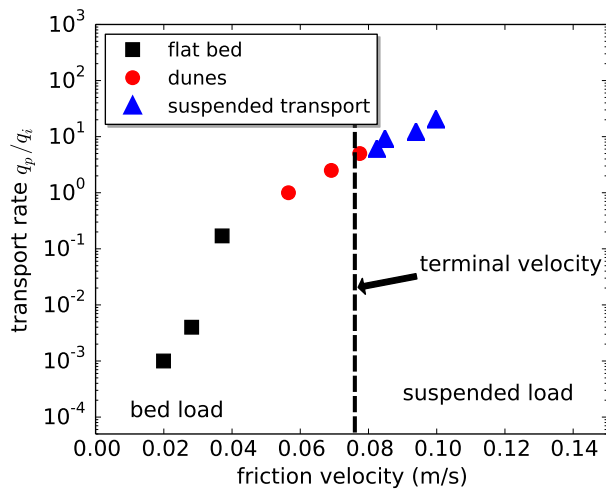


Figure 16: The regime of sediment transport obtained by using CFD–DEM. The vertical line is drawn according to Bagnold criterion.

### 5.3. Coexistence of Bedload and Suspended Load

Calculations of sediment transport in engineering practice have assume either bedload or suspended load depending on which mode is dominating. Whether or to what extent the two transport modes can co-exist is an open question that is subject to debate. CFD–DEM simulations have the potential to shed light on this issue. A typical snapshot taken from the Case 3 with  $U_b = 1.2m/s$  is presented in Fig. 17(a), with the bedload and suspended load separated based on two different criteria based on particle velocity (panel b) and particle concentration (panel c) of two threshold values. It can be seen in the figure that there is a layer of approximately  $10d_p$  of particles moving slowly as bedload at high Shields parameter.



In our study, we use a threshold of particle velocity  $u_x < 3u_{term}$  to separate bedload from suspended load according to the maximum particle velocity in bedload transport (Schmeeckle, 2014), where particle terminal velocity  $u_{term} = 0.077$  m/s. The threshold of the solid volume fraction  $\varepsilon_s$  is also used to capture bedload sediment transport, which is shown in Fig. 17(c). Indeed, the figure suggests that the specific fractions of bedload and suspended load depend on the criterion used to delineate them (i.e., based on particle velocity or particle volume fraction) and on the threshold values (e.g.,  $\epsilon_{s} = 0.1$  or  $0.3$ ). However, it is clear that regardless of the criterion or threshold value adopted, bedload and suspended load co-exist in the snapshot analyzed, and both account for significant portion of the total sediment flux.

The empirical formulas calibrated on experiments primarily consisting of bedload can be very inaccurate when used to predict flows with suspended load or a mixture of the transport modes, vice versa for formulas developed for suspended load. This is illustrated in Fig. 18, which shows revisions of the formula of Meyer-Peter and Müller (1948) obtained by Wong and Parker (2006) and Nielsen (1992) are applied to predict the sediment transport rate at different regimes. The prediction of the sediment transport rate by the revised equation proposed by Wong and Parker (2006) is based on the bedload and is significantly smaller than the prediction of Nielsen (1992). To investigate the differences between different revisions of the Meyer-Peter and Müller formula, we separated bedload and suspended load using the threshold particle velocity  $3u_{term}$  and plotted them as a function of the Shields parameter in Fig. 18. It can be seen from Fig. 18 that the bedload agrees with the formula proposed by Wong and Parker (2006), and the suspended load agrees with the formula proposed by Nielsen (1992). Therefore, the deviation of the coefficient in different revisions of Meyer-Peter and Müller formula is due to the significant increase of sediment transport rate from suspended load.

## 6. Conclusion

In this work, a comprehensive study of current-induced sediment transport in a wide range of regimes is performed by using CFD-DEM solver *SediFoam*. Detailed quantitative comparisons are performed using the results obtained in the present simulations and those

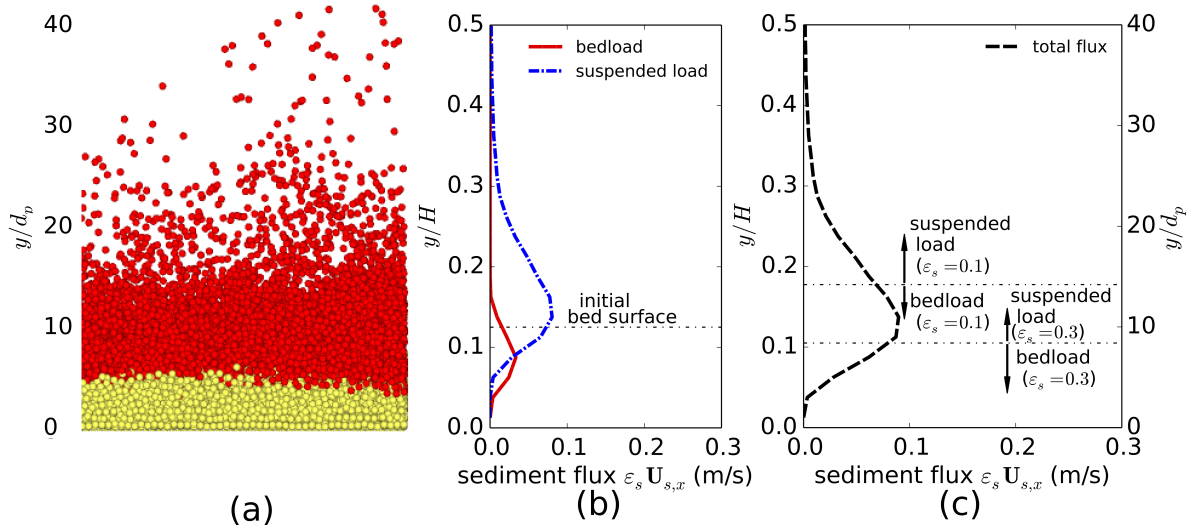


Figure 17: Comparison of bedload and suspended load in Case 3 at  $U_b = 1.2$  m/s. Particles moving at  $u_x > 3u_{term}$  are considered as suspended particle and colored by red in the left panel; particles moving at  $u_x \leq 3u_{term}$  are considered as bedload and colored by yellow in the left panel. Panel (a) and (b) are the comparisons of the vertical profiles of bedload flux and suspended load flux. The middle panel uses a threshold particle velocity at  $u_x \leq 3u_{term}$  to capture the bedload; the right panel uses threshold solid volume fraction values of 0.1 and 0.3. The initial sediment bed is approximately  $10d_p$ , which corresponds to  $y/H = 0.125$ .

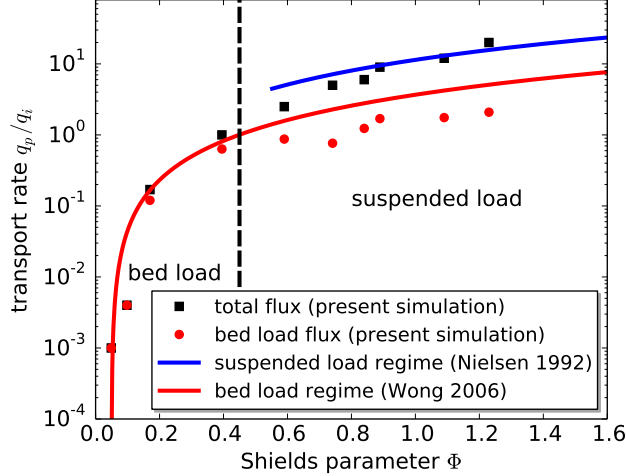


Figure 18: Comparison of the bedload flux and total flux in the present simulations. The particles moving at  $u_x > 3u_{term}$  are considered as suspended particle, where  $u_{term} = 0.077$  m/s is the terminal velocity of the sediment particle.

in the literature. It is demonstrated from the comparison that the accuracy of CFD–DEM is satisfactory for the simulation of different sediment bed patterns. Considering the computational cost of CFD–DEM is much smaller than that of the interface-resolved method, CFD–DEM is promising in the simulation of sediment transport. This opens up the possibility to apply CFD–DEM to investigate realistic sediment transport problems, e.g., the formation of ripples in the wave.

In addition, the improvement of the results over existing CFD–DEM simulations is demonstrated. We used a computational domain that is large enough to incorporate the bed form (ripples), which is important advance over the featureless bed in the studies by Schmeekle (2014). The second improvement of the present model is the averaging algorithm, which enables mass conservation and resolves the boundary layer fluid flow simultaneously. Third, we used a drag formulation that considered the influence of the volume fraction, which improves the prediction of the sediment flux in suspended load. Finally, we considered the influence of additional forcing terms in our numerical simulations, including added mass and lift force. Because of the improvements, the sediment transport rate in the suspended load regime agrees better with the experimental results when the solid volume

fraction is considered. Moreover, reasonable predictions of the friction coefficient  $C_f$  and the fluid flow at the sediment bed are reported.

## 7. Acknowledgment

The computational resources used for this project were provided by the Advanced Research Computing (ARC) of Virginia Tech, which is gratefully acknowledged. We thank Dr. Kidanemariam for the discussion that helped the numerical simulations in the present paper. We thank the anonymous reviewers for their comments, which helped improve the quality of the manuscript. The authors gratefully acknowledge partial funding of graduate research assistantship from the Institute for Critical Technology and Applied Science (ICTAS, Grant number 175258).

## 8. Reference

### References

- Anderson, T., Jackson, R., 1967. A fluid mechanical description of fluidized beds: Equations of motion. *Industrial and Chemistry Engineering Fundamentals* 6, 527–534.
- Arolla, S. K., Desjardins, O., 2015. Transport modeling of sedimenting particles in a turbulent pipe flow using Euler–Lagrange large eddy simulation. *International Journal of Multiphase Flow* 75, 1 – 11.
- Aussillous, P., Chauchat, J., Pailha, M., Médale, M., Guazzelli, E., 2013. Investigation of the mobile granular layer in bedload transport by laminar shearing flows. *Journal of Fluid Mechanics* 736, 594–615.
- Bagnold, R. A., 1966. An approach to the sediment transport problem from general physics. *Geological Survey Professional Paper* 422 (1), 1–37.
- Ball, R. C., Melrose, J. R., 1997. A simulation technique for many spheres in quasi-static motion under frame-invariant pair drag and Brownian forces. *Physica A: Statistical Mechanics and its Applications* 247 (1), 444–472.

- Brownlie, W. R., 1982. Prediction of flow depth and sediment discharge in open channels. Ph.D. thesis, California Institute of Technology.
- Calantoni, J., Holland, K. T., Drake, T. G., 2004. Modelling sheet-flow sediment transport in wave-bottom boundary layers using discrete-element modelling. *Philosophical Transactions of Royal Society of London: Series A* 362, 1987–2002.
- Capecelatro, J., Desjardins, O., 2013. An Euler–Lagrange strategy for simulating particle-laden flows. *Journal of Computational Physics* 238, 1–31.
- Charru, F., Hinch, E., 2006. Ripple formation on a particle bed sheared by a viscous liquid. Part 1. steady flow. *Journal of Fluid Mechanics* 550, 111–121.
- Cundall, P., Strack, D., 1979. A discrete numerical model for granular assemblies. *Géotechnique* 29, 47–65.
- Delft Hydraulics, 1999. User manual Delft3D-FLOW. WL|Delft Hydraulics, The Netherlands.
- Drake, T. G., Calantoni, J., 2001. Discrete particle model for sheet flow sediment transport in the nearshore. *Journal of Geophysical Research: Oceans* (1978–2012) 106 (C9), 19859–19868.
- Durán, O., Andreotti, B., Claudin, P., 2012. Numerical simulation of turbulent sediment transport, from bed load to saltation. *Physics of Fluids* (1994-present) 24 (10), 103306.
- Ebrahimi, M., 2014. CFD-DEM modelling of two-phase pneumatic conveying with experimental validation. Ph.D. thesis, The University of Edinburgh.
- Feng, Y., Yu, A., 2007. Microdynamic modelling and analysis of the mixing and segregation of binary mixtures of particles in gas fluidization. *Chemical Engineering Science* 62 (1-2), 256–268.

- Goniva, C., Kloss, C., Pirker, S., 12-13 November 2009. Towards fast parallel CFD–DEM: an open-source perspective. In: Open Source CFD International Conference, Barcelona, Spain.
- Han, T., Levy, A., Kalman, H., 2003. DEM simulation for attrition of salt during dilute-phase pneumatic conveying. *Powder Technology* 129 (1), 92–100.
- Hsu, T.-J., Jenkins, J. T., Liu, P. L.-F., 2004. On two-phase sediment transport: sheet flow of massive particles. *Proceedings of the Royal Society of London A: Mathematical, Physical and Engineering Sciences* 460 (2048), 2223–2250.
- Issa, R. I., 1986. Solution of the implicitly discretised fluid flow equations by operator-splitting. *Journal of Computational Physics* 62 (1), 40–65.
- Jasak, H., 1996. Error analysis and estimation for the finite volume method with applications to fluid flows. Ph.D. thesis, Imperial College London (University of London).
- Jiang, Z., 1995. The motion of sediment-water mixtures during intense bedload transport: computer simulations. *Sedimentology* 42 (6), 935–945.
- Kafui, K., Thornton, C., Adams, M., 2002. Discrete particle–continuum fluid modelling of gas–solid fluidised beds. *Chemical Engineering Science* 57 (13).
- Kempe, T., Fröhlich, J., 2012. Collision modelling for the interface-resolved simulation of spherical particles in viscous fluids. *Journal of Fluid Mechanics* 709, 445–489.
- Kempe, T., Vowinckel, B., Fröhlich, J., 2014. On the relevance of collision modeling for interface-resolving simulations of sediment transport in open channel flow. *International Journal of Multiphase Flow* 58, 214–235.
- Kidanemariam, A. G., Uhlmann, M., 2014a. Direct numerical simulation of pattern formation in subaqueous sediment. *Journal of Fluid Mechanics* 750, R2.

- Kidanemariam, A. G., Uhlmann, M., 2014b. Interface-resolved direct numerical simulation of the erosion of a sediment bed sheared by laminar channel flow. *International Journal of Multiphase Flow* 67, 174–188.
- Kloss, C., Goniva, C., Hager, A., Amberger, S., Pirker, S., 2012. Models, algorithms and validation for opensource DEM and CFD–DEM. *Progress in Computational Fluid Dynamics, an International Journal* 12 (2), 140–152.
- Lesser, G., van Kester, J., Roelvink, J., 2000. Online sediment transport within Delft3D-FLOW. Delft, the Netherlands: WL|Delft Hydraulics, Report Z-2899.
- Meyer-Peter, E., Müller, R., 1948. Formula for bed load transport. In: *Proceedings of the 2nd meeting of the International Association for Hydraulic Structures Research*, Stockholm. pp. 39–64.
- Nabi, M., Vriend, H., Mosselman, E., Sloff, C., Shimizu, Y., 2013. Detailed simulation of morphodynamics: 3. ripples and dunes. *Water resources research* 49 (9), 5930–5943.
- Nielsen, P., 1992. Coastal bottom boundary layers and sediment transport. World Scientific Publishing, Singapore.
- OpenCFD, 2013. OpenFOAM User Guide. See also <http://www.opencfd.co.uk/openfoam>.
- Ouriemi, M., Aussillous, P., Guazzelli, E., 2009. Sediment dynamics. Part 2. Dune formation in pipe flow. *Journal of Fluid Mechanics* 636, 321–336.
- Plimpton, J., 1995. Fast parallel algorithms for short-range molecular dynamics. *J. Comp. Phys.* 117, 1–19, see also <http://lammmps.sandia.gov/index.html>.
- Rusche, H., 2003. Computational fluid dynamics of dispersed two-phase flows at high phase fractions. Ph.D. thesis, Imperial College London (University of London).
- Saffman, P., 1965. The lift on a small sphere in a slow shear flow. *Journal of fluid mechanics* 22 (02), 385–400.

- Schmeeckle, M. W., 2014. Numerical simulation of turbulence and sediment transport of medium sand. *Journal of Geophysical Research: Earth Surface* 119, 1240–1262.
- Smith, D. A., Cheung, K. F., 2004. Initiation of motion of calcareous sand. *Journal of Hydraulic Engineering* 130 (5), 467–472.
- Sun, J., Battaglia, F., Subramaniam, S., 2007. Hybrid two-fluid DEM simulation of gas-solid fluidized beds. *Journal of Fluids Engineering* 129 (11), 1394–1403.
- Sun, R., Xiao, H., 2015a. Diffusion-based coarse graining in hybrid continuum–discrete solvers: Applications in CFD–DEM. *International Journal of Multiphase Flow* 72, 233–247.
- Sun, R., Xiao, H., 2015b. Diffusion-based coarse graining in hybrid continuumdiscrete solvers: Theoretical formulation and a priori tests. *International Journal of Multiphase Flow* 77, 142 – 157.
- Sun, R., Xiao, H., 2016. Sedifoam: A general-purpose, open-source CFD-DEM solver for particle-laden flow with emphasis on sediment transport. *Computers & Geosciences*. Accepted. DOI:<http://dx.doi.org/10.1016/j.cageo.2016.01.011> Available at <http://arxiv.org/abs/arXiv:1601.03801>.
- Syamlal, M., Rogers, W., O'Brien, T., 1993. MFIx documentation: Theory guide. Tech. rep., National Energy Technology Laboratory, Department of Energy, see also URL <http://www.mfix.org>.
- Tsuji, Y., Kawaguchi, T., Tanaka, T., 1993. Discrete particle simulation of two-dimensional fluidized bed. *Powder Technology* 77 (79-87).
- van Rijn, L., 1984. Sediment transport, part I: Bed load transport. *Journal of hydraulic engineering* 110 (10), 1431–1456.
- Warren, I., Bach, H., 1992. MIKE 21: a modelling system for estuaries, coastal waters and seas. *Environmental Software* 7 (4), 229–240.



- Wong, M., Parker, G., 2006. Reanalysis and correction of bed-load relation of meyer-peter and müller using their own database. *Journal of Hydraulic Engineering* 132 (11), 1159–1168.
- Xiao, H., Young, Y. L., Prévost, J. H., 2010. Hydro- and morpho-dynamic modeling of breaking solitary waves over sand beach. Part II: Numerical simulation. *Marine Geology* 269, 119–131.
- Yoshizawa, A., Horiuti, K., 1985. A statistically-derived subgrid-scale kinetic energy model for the large-eddy simulation of turbulent flows. *Journal of the Physical Society of Japan* 54 (8), 2834–2839.
- Yu, X., Hsu, T.-J., Jenkins, J. T., Liu, P. L.-F., 2012. Predictions of vertical sediment flux in oscillatory flows using a two-phase, sheet-flow model. *Advances in Water Resources* 48, 2–17.
- Zedler, E. A., Street, R. L., 2001. Large-eddy simulation of sediment transport: currents over ripples. *Journal of Hydraulic Engineering* 127 (6), 444–452.
- Zhou, Z., Pinson, D., Zou, R., Yu, A., 2011. Discrete particle simulation of gas fluidization of ellipsoidal particles. *Chemical Engineering Science* 66 (23), 6128–6145.